

SUPPLEMENTAL MATERIAL

Stability of a liquid jet impinging a confined saturated sand

J. Vessaire, G. Varas, S. Joubaud, R. Volk, M. Bourgoïn & V. Vidal

A.1 Crater morphology

Figure S1 displays the temporal evolution of the crater depth D and width L , this latter being computed at the altitude used for fluxes computation (core of the crater, red line Fig.1c,d). After a rapid transient, the crater morphology only evolves slowly in time. A logarithmic function described well this slow evolution (black lines, guides for the eyes), as already reported in the literature [Metger et al., 2009; Clark & Behringer, 2014; Badr et al., 2014].

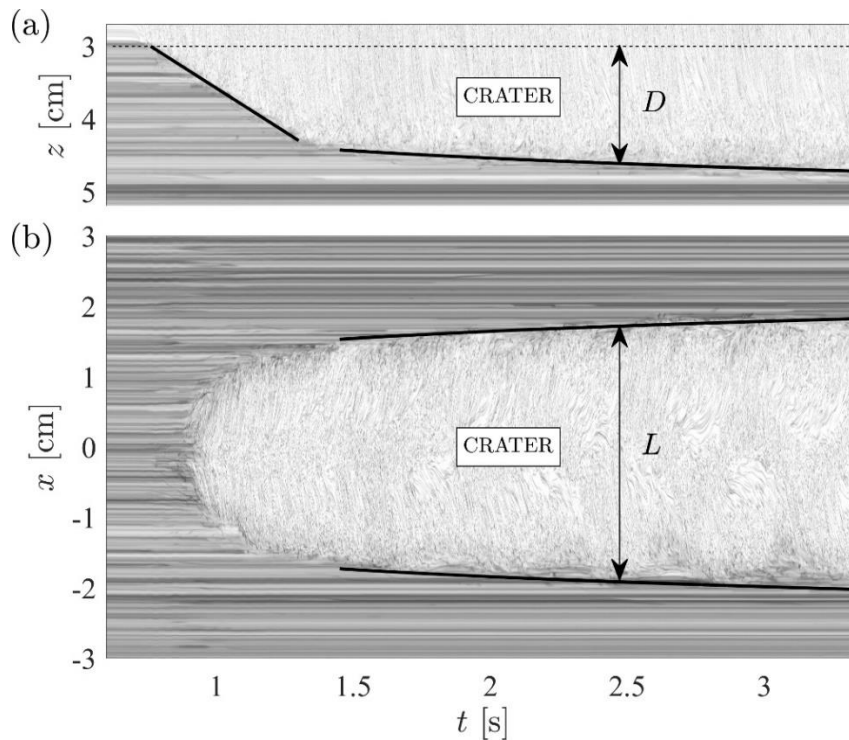


Figure S1: Spatiotemporal evolution of the crater depth D (a) and width L (b) at the altitude where the fluxes are computed (red line, Fig.1c) [$h = 3$ cm, $Q = 4$ mL/s].

A.2 Jet indentation

For low h and Q , we report a peculiar regime of jet indentation. In this case, the jet digs the granular layer and forms a thin, elongated crater of small depth (Figure S2). This morphology is not relevant for our study, which focuses on larger craters, and is therefore not shown in the main text. Note that this case corresponds to the Strongly Deflected Jet Regime I (SDJR 1) described by Aderibidge & Rajaratnam (1996).

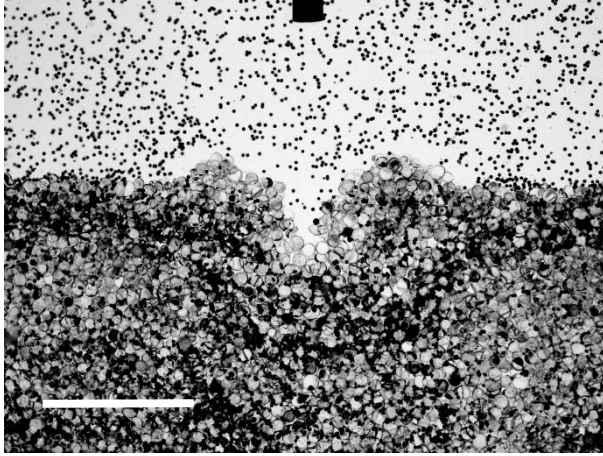


Figure S2: Peculiar case of jet indentation for small (h, Q) [$h = 1$ cm, $Q = 0.4$ mL/s]. The injection nozzle is visible in black at the top of the image. The white bar represents 1 cm.

A.3 Movies

The movies corresponding to the four examples displayed in Figure 1 are provided as the following additional files. For each set of parameter (h, Q) , run 0 is shown (5 experimental runs in total). Movies are slowed down (x1/4).

[Movie1_h=3cm_Q=04mLs.mp4](#)

[Movie2_h=3cm_Q=1mLs.mp4](#)

[Movie3_h=3cm_Q=2mLs.mp4](#)

[Movie4_h=3cm_Q=4mLs.mp4](#)

Movie 1 displays the case of weak erosion (Fig.1a,e). Although weak erosion is not able to dig a crater at the granular bed surface, it is able to move a few grains, and is therefore distinguished from “no erosion”, for which the jet does not move any grains. Movie 2 shows an open crater (Fig.1b,f). Movies 3 and 4 show close craters (Fig.1c,g and Fig.1d,h). The close crater in Movie 3 is distinguished from the open crater in Movie 2 as it displays vertical or overhanging walls (in addition to the absence of buckling streamlines outside the crater which characterize the open craters).

A.4 Jet angle

The half-angle α of the jet for given parameters (h, Q) was measured in the absence of a granular layer, h corresponding here to the distance between the injection nozzle and the cell bottom (horizontal wall). The goal here is to provide an estimate of the impact zone of the jet from its aperture angle, a full study of the jet behavior in this geometry being out of the scope of this work.

The PIV spatial resolution is adapted to the tracer concentration and is not enough, by itself, to provide a precise measurement of the jet angle. We perform the average of the last 1000 images in the stationary regime (similarly to Fig.1, lower panel). On these time-averaged images, the jet boundaries appear clearly as an abrupt change of contrast on the gray intensity scale (Figure S4a). We then picked manually the jet angle from the superposition of the time-averaged images and the PIV mean field (this latter being used as a guideline). The errors were estimated as follows:

- 1) The error due to both the manual pointing and the fluctuations of the jet boundaries (which does not have perfectly straight borders) is accounted for by picking systematically the minimum and maximum jet angle (dashed red and black lines in Figure S4a).
- 2) Errors due to the experimental repeatability are computed by estimating α for 3 different experimental runs with the jet alone in the same experimental configuration (h, Q).

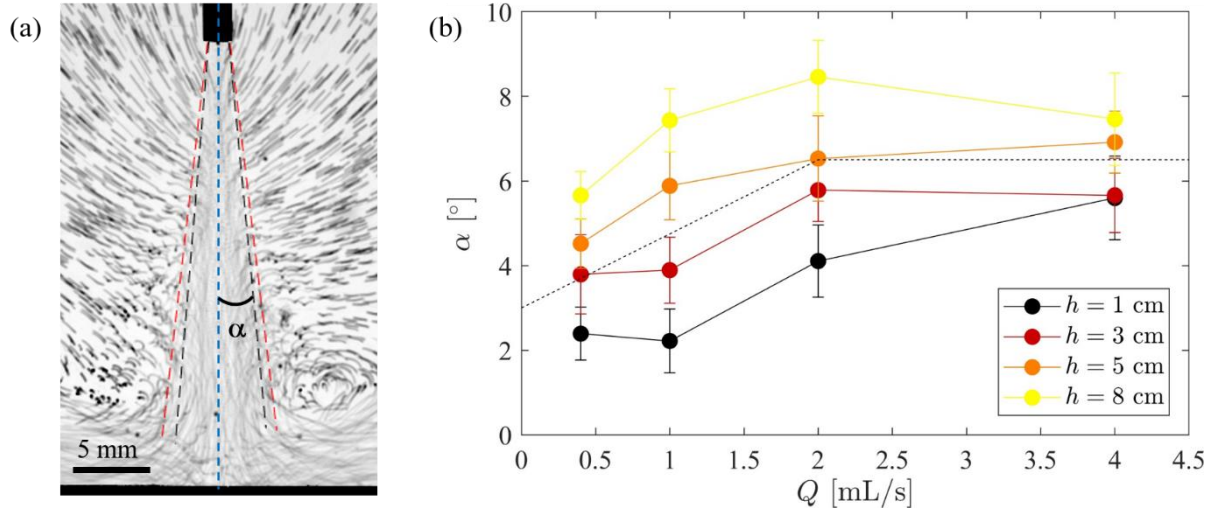


Figure S4: Determination of the jet half-angle α . (a) Example of pointing the maximum (dashed red) and minimum (dashed black) angle [$h = 3$ cm, $Q = 2$ mL/s]. (b) Jet half-angle α as a function of Q for different h . The errorbars indicate the minimum (lower) and maximum (higher) value of α taken from (a) and averaged on the 3 experimental runs. The dashed line indicates the average angle evolution as a function of the flow rate, $\alpha = \alpha_0 + (\alpha^* - \alpha_0) \cdot Q/Q_c$, with $\alpha_0 = 2^\circ$, $\alpha^* = 6.5^\circ$ and $Q_c = 2$ mL/s (see text).

Figure S4b displays the jet half-angle, α , as a function of the injection flow-rate, Q , for different h . We report a slight increase as a function of Q and h . The average value and minimum/maximum values of α are used to compute the boundaries (solid black and dashed gray lines) in the regime diagram (Figure 2). To do so, we use equation (1) with $J=0.6$, a critical value for the transition to soil erosion already proposed in the literature [Aderibigbe & Rajaratnam, 1996]. For each h , the critical value of Q is then computed from the equation based on the experimental values for $\tan(\alpha(h, Q))$ reported in Figure S4b. No solution is found for $h=1$ cm, which may be due to the peculiar crater geometry in this configuration (indentation, see section A.2). Due to the experimental uncertainties in the determination of α , we consider its average evolution as a function of the flow rate, $\alpha = \alpha_0 + (\alpha^* - \alpha_0) \cdot Q/Q_c$, with $\alpha_0 = 2^\circ$, $\alpha^* = 6.5^\circ$ and $Q_c = 2$ mL/s (dashed line, Figure S4b) to estimate J in Figures 3 and 4.

References

- O.O. Aderibigbe & N. Rajaratnam, *Journal of Hydraulic Research*, **34**:1, 19-33 (1996).
 S. Badr, G. Gauthier, P. Gondret, *Physics of Fluids* **26**(2), 023302 (2014).
 A.H. Clark, R.P. Behringer, *Granular Matter* **16**(4), 433 (2014).
 P.T. Metzger, R.C. Latta, J.M. Schuler, C.D. Immer, *AIP Conference Proceedings* **1145**(1), 767 (2009).